Verification and Validation of HiFiLES: a High-Order Navier-Stokes unstructured solver on multi-GPU platforms

Manuel R. López-Morales *, Abhishek Sheshadri,†,
Kartikey Asthana†, Jonathan Bull‡, Jacob Crabill§, Thomas Economon†, David Manosalvas†,
Joshua Romero†, Jerry Watkins†, David Williams¶,
Francisco Palacios‖, and Antony Jameson**

Department of Aeronautics and Astronautics, Stanford University, Stanford, CA, 94305

The goal of this paper is to show a detailed Verification and Validation of HiFiLES: a high-order Navier-Stokes solver developed at the Aerospace Computing Laboratory (ACL) at Stanford University. HiFiLES has been built on top of SD++ (Castonguay et al.) and achieves high-order spatial discretization with the Energy-Stable Flux Reconstruction (ESFR) scheme in unstructured grids (two and three dimensions). The high parallelizability of this scheme motivates the optimization of the solvers ability to run in a multi-GPU (Graphical Processing Unit) environment. We intend this paper to be the main reference for HiFiLES and serve as a sort of manual for researchers and engineers that would like to develop or implement high-order numerical schemes based on an Energy-Stable Flux Reconstruction (ESFR) scheme.

I. Introduction

Over the last 20 years, much fundamental work has been done in developing high-order numerical methods for Computational Fluid Dynamics. Moreover, the need to improve and simplify these methods has attracted the interest of the applied mathematics and the engineering communities. Now, these methods are beginning to prove themselves sufficiently robust, accurate and efficient for use in real-world applications.

However, low-order numerical methods are still the standard in aeronautical industry. There has been a sustained scientific and economical investment to develop this successful and robust technology for a long time. Currently, a state-of-the-art 2nd-order Finite Volume computational tool performs adequately well in a broad range of aeronautical engineering applications. For that reason, the introduction of brand new high-order numerical schemes in the aeronautical industry is challenging, particularly in areas where the low-order numerical methods already provide the required robustness and accuracy (keeping in mind the limitations of the current turbulence model technology).

Thanks to new and emerging aircraft roles (very small or very big concepts, very high or very low altitude, quiet vehicles, low fuel consumption, etc.), revolutionary aircraft design concepts will appear in the near future and the need for high-fidelity simulation techniques to predict their performance is growing rapidly. Undoubtedly, high-order numerical methods are starting to find their place in the aeronautical industry.

Unsteady simulation, flapping wings, wake capturing, noise prediction and Large Eddy Simulations are just a few examples of computations that require high-order numerical methods. In particular, high-order methods have a significant edge in applications that require accurate resolution of the smallest scales of the flow. Such situations include the generation and propagation of acoustic noise from the airframe, or at the limits of the flight envelope where unsteady vortex-dominated flows have a significant effect on the aircraft's performance. Utilizing a high-order representation enables the smallest scales to be represented with a greater degree of accuracy than standard second-order methods. Furthermore, high-order methods are inherently less dissipative, resulting in less unwanted interference

*Ph.D. Candidate, Department of Aeronautics and Astronautics, Stanford University, AIAA Student Member; mlopez14@stanford.edu
†Ph.D. Candidates (authors in alphabetical order), Department of Aeronautics and Astronautics, AIAA Student Members
‡Postdoctoral Scholar, Department of Aeronautics and Astronautics, Stanford University, AIAA Member
§M.S. Student, Department of Aeronautics and Astronautics, Stanford University, AIAA Student Member
¶CFD Engineer, Flight Sciences Division, Boeing Commercial Airplanes, AIAA Member
‖Engineering Research Associate, Department of Aeronautics and Astronautics, AIAA Senior Member
**Thomas V. Jones Professor of Engineering, Department of Aeronautics and Astronautics, Stanford University, AIAA Fellow

with the correct development of the turbulent energy cascade.

Finally, the amount of computing effort to achieve a small error tolerance can be much smaller with high-order than second-order methods. Even real time simulations (one second of computational time, one second of real flight), could benefit from high-order algorithms which count on a more intensive inner element computation (ideal for vector machines and new computational platforms like GPUs, FPGAs, coprocessors, etc).

But, before claiming the future success of the high-order numerical methods in the industry, two main difficulties should be overcome: a) high-order numerical schemes must be as robust as a state-of-the-art low-order numerical method. b) the existing level of Verification and Validation (V&V) in high-order CFD codes should be similar to the typical level of their low-order counterparts.

During the last decade, the Aerospace Computing Laboratory (ACL) of the Department of Aeronautics and Astronautics at Stanford University has developed a series of high-order numerical schemes and computational tools, contributing massively to the demonstration of the viability of this technique. In this paper, a code called HiFiLES developed at ACL and built on top of SD++ (Castonguay et al.[1]) is described in detail with a particular emphasis on robustness in a broad range of applications and an industrial-like level of V&V. HiFiLES takes advantage of the synergies between applied mathematics, aerospace engineering, and computer science to achieve the ultimate goal of developing an advanced high-fidelity simulation environment.

Apart from the original characteristics of the SD++ code (described in Castonguay et al.[1]), HiFiLES includes some important physical models and computational methods such as: Large Eddy Simulation (LES) using explicit filters and advanced subgrid-scale (SGS) models, high-order stabilization techniques, shock detection and capturing for compressible flow calculations, convergence acceleration methodologies like p-multigrid, and local and dual time stepping.

During the development of this software several key decisions have been taken to guarantee a flexible and lasting infrastructure for industrial Computational Fluid Dynamics simulations:

- The selection of the Energy-Stable Flux Reconstruction (ESFR) scheme on unstructured grids. The flexibility of this method has been critical to guarantee a correct solution independently of the particular physical characteristics of the problem.
- High performance, materialized in a multi-GPU implementation which takes advantage of the ease of parallelization afforded by discontinuous solution representation. Furthermore, HiFiLES aims to guarantee compatibility with future vector machines and revolutionary hardware technologies.
- Code portability by using ANSI C++ and relying on widely-available, and well-supported mathematical libraries like Blas, LAPACK, CuBLAS and ParMetis.
- Object oriented structure to boost the re-usability and encapsulation of the code. This abstraction enables modifications without incorrectly affecting other portions of the code. Although some level of performance is traded for re-usability and encapsulation, the loss in performance is minor.

As mentioned before, the mathematical basis and computational implementation of HiFiLES were described in Castonguay et al. For that reason, the goal of this paper is to illustrate the level of robustness of HiFiLES in complex problems, via a detailed Verification and Validation study which is fundamental to increase the credibility of this technology in a competitive industrial framework.

In particular, to ensure that the implementation of the aforementioned features in HiFiLES is correct, the following verification tests will be shown in the final version of this paper: checks of spatial and temporal order of accuracy using the Method of Manufactured Solutions (MMS) in 2D and 3D for viscous and inviscid flows, characterization of stable time-step limits, assessment of computational cost per degree of freedom for a given error tolerance, and measurement of weak and strong scalability in GPUs and CPUs.

After the Verification, a detailed Validation of the code will be presented to illustrate that the solutions provided by HiFiLES are an accurate representation of the real world. Simulations of complex flows will be validated against experimental or Direct Numerical Simulation (DNS) results for the following cases: laminar and turbulent flat plane, flow around a circular cylinder, subsonic flow attached in a NACA0012, SD7003 wing-section and airfoil at $4°$ angle of attack, LES of the Taylor-Green Vortex, and DNS and LES of Decaying Homogeneous Turbulence.

The organization of this paper is as follows. Section II. provides a description of the governing equations. Section III. describes the mathematical numerical algorithms implemented in the code (with a particular emphasis in convergence acceleration techniques and stability). IV. and V. focus on the Verification and Validation of HiFiLES, and finally, the conclusions are summarized in section VI..

Finally, it is our intent for this paper to be the main reference for work that uses or enhances the capabilities of HiFiLES, and for it to serve as a sort of reference for researchers and engineers that would like to develop or implement High-order numerical schemes based on an Energy-Stable Flux Reconstruction (ESFR) scheme.

II. Governing Equations

In this article, we are concerned with time-accurate, viscous flow around aerodynamic bodies in arbitrary motion which is governed by the compressible, unsteady Navier-Stokes (NS) equations. Consider the equations in a domain, $\Omega \subset \mathbf{R}^3$, with a disconnected boundary that is divided into a far-field component, Γ_∞, and an adiabatic wall boundary. The surface S represents the outer mold line of an aerodynamic body, and it is considered continuously differentiable (C^1). These conservation equations along with a generic source term, $\mathcal{Q}$, can be expressed in an arbitrary Lagrangian-Eulerian (ALE) differential form as

$$\begin{cases} \mathcal{R}(U) = \frac{\partial U}{\partial t} + \nabla \cdot \vec{F}^c_{ale} - \nabla \cdot (\mu^1_{tot} \vec{F}^{v1} + \mu^2_{tot} \vec{F}^{v2}) - \mathcal{Q} = 0, & \text{in } \Omega, \quad t > 0 \\ \vec{v} = \vec{u}_\Omega, & \text{on } S, \\ \partial_n T = 0, & \text{on } S, \\ (W)_+ = W_\infty, & \text{on } \Gamma_\infty, \end{cases} \tag{1}$$

where

$$U = \left\{ \begin{array}{c} \rho \\ \rho \vec{v} \\ \rho E \end{array} \right\}, \vec{F}^c_{ale} = \left\{ \begin{array}{c} \rho(\vec{v} - \vec{u}_\Omega) \\ \rho \vec{v} \otimes (\vec{v} - \vec{u}_\Omega) + \bar{\bar{I}} p \\ \rho E(\vec{v} - \vec{u}_\Omega) + p\vec{v} \end{array} \right\}, \vec{F}^{v1} = \left\{ \begin{array}{c} \cdot \\ \bar{\bar{\tau}} \\ \bar{\bar{\tau}} \cdot \vec{v} \end{array} \right\}, \vec{F}^{v2} = \left\{ \begin{array}{c} \cdot \\ \cdot \\ c_p \nabla T \end{array} \right\}, \mathcal{Q} = \left\{ \begin{array}{c} q_\rho \\ \vec{q}_{\rho \vec{v}} \\ q_{\rho E} \end{array} \right\}, \tag{2}$$

$$\bar{\bar{\tau}} = \nabla \vec{v} + \nabla \vec{v}^{\mathsf{T}} - \frac{2}{3} \bar{\bar{I}} (\nabla \cdot \vec{v}). \tag{3}$$

$$p = (\gamma - 1)\rho \left[E - \frac{1}{2} (\vec{v} \cdot \vec{v}) \right], \tag{4}$$

and the temperature is given by

$$T = \frac{p}{\rho R}. \tag{5}$$

III. Numerics

A. Flux Reconstruction Method

What follows is an overview of the flux reconstruction (FR) framework. We start the discussion with the solution of the advection equation in one dimension using the FR approach to illustrate the peculiarities of the method. Then we proceed to describe the solution of the advection in two and three dimensions to show how the scheme works in triangular and tetrahedral elements. More details about FR and ESFR properties and derivations can be found in the articles and papers by Williams, Vincent, Castonguay, Jameson, and Huynh.

1. Solution of the Advection Equation in One Dimension using the FR Approach

Consider the one-dimensional conservation law

$$\frac{\partial u}{\partial t} + \frac{\partial f}{\partial x} = 0 \tag{6}$$

in domain Ω, where x is the spatial coordinate, t is time, u is a scalar function of x and t, and f is a scalar function of u. Note that letting $f = f(u, \frac{\partial u}{\partial x})$, Equation6 becomes a model of the Navier-Stokes equations.

Let us partition the domain $\Omega = [x_1, x_{N+1})$ into N non-overlapping elements with interfaces at $x_1 < x_2 < ... < x_{N+1}$. Then,

$$\Omega = \bigcup_{n=1}^{N} \Omega_n$$

and $\Omega_n = [x_n, x_{n+1})$ for $n = 1, ..., N$.

To simplify the implementation, let us map each of the physical elements Ω_n to a standard element $\Omega_s = [-1, 1)$ with the function $\Theta_n(\xi)$, where

$$x = \Theta_n(\xi) = \left(\frac{1-\xi}{2}\right) x_n + \left(\frac{1+\xi}{2}\right) x_{n+1}$$

With this mapping, the evolution of u within each Ω_n can be determined with the following transformed advection equation

$$\frac{\partial \hat{u}}{\partial t} + \frac{\partial \hat{f}}{\partial \xi} = 0$$

where

$$\hat{u} = J_n u(\Theta_n(\xi), t) \text{ in } \Omega_n$$

$$\hat{f} = f(\Theta_n(\xi), t) \text{ in } \Omega_n$$

Now, introduce polynomial approximations $\hat{u}^\delta$, $\hat{f}^\delta$ to the exact values $\hat{u}$, $\hat{f}$, respectively. Using piecewise polynomials of degree p as approximations, we can write

$$\hat{u}^\delta = \sum_{i=1}^{N_s} \hat{u}_i^\delta l_i(\xi)$$

$$\hat{f}^\delta = \sum_{i=1}^{N_s} \hat{f}_i^\delta l_i(\xi)$$

where N_s is the number of solution points, $\hat{u}_i^\delta$ is the current value of the solution approximation function at the i^{th} solution point in the reference element, $\hat{f}_i^\delta$ is the current value of the flux approximation function at the i^{th} solution point in the reference element, l_i is the Lagrange polynomial equal to 1 at the i^{th} solution point and 0 in the others, and δ signals that the function is an approximation.

Note that the piecewise polynomials may not be continuous (or c_0) accross the interfaces. In the Flux Reconstruction approach, the flux used in the time advancement of the solution is made c_0 by introducing flux correction functions. To this end, in the general non-linear advection case, it is necessary to first make the solution c_0.

This can be done by finding interface values at each element and then correcting the solution. Let $\hat{u}_L^{\delta I}$ and $\hat{u}_R^{\delta I}$ be the interface values at left and right boundaries of each element, respectively. Then, select solution correction functions g_L and g_R such that

$$g_L(-1) = 1 \; g_L(1) = 0$$

$$g_R(-1) = 0 \; g_R(1) = 1$$

and let

$$\hat{u}^c = \hat{u}^\delta + (\hat{u}_L^{\delta I} - \hat{u}_L^\delta) g_L + (\hat{u}_R^{\delta I} - \hat{u}_R^\delta) g_R$$

where superscript c denotes the function is corrected, and $\hat{u}_L^\delta$, $\hat{u}_R^\delta$ represent the solution approximation evaluated at the left and right boundaries.

We can proceed in a similar fashion to correct the flux to obtain

$$\hat{f}^c = \hat{f}^\delta + (\hat{f}_L^{\delta I} - \hat{f}_L^\delta) h_L + (\hat{f}_R^{\delta I} - \hat{f}_R^\delta) h_R$$

where h_R and h_L are right and left flux correction functions satisfying the same boundary conditions as g_R and g_L, respectively.

The solution can then be advanced at each solution point. In semi-discrete form, this is

$$\frac{d\hat{u}_i^\delta}{dt} = -\frac{\partial \hat{f}^c}{\partial \xi}(\xi_i)$$

The FR scheme can be made stable by selecting special types of correction functions.

B. Unstructured Mesh Treatment

Mention developments in squares (tensor products of linear scheme), triangles[2,3], tetrahedra[4], prisms (tensor product of linear with triangular schemes), and hexahedra (tensor products of linear scheme).

C. Time Stepping and p-multigrid

Explicit RK4 with ability to use multigrid[5] and dual time-stepping[6] for implicit time advancement.

D. Large Eddy Simulation Models

SGS Models: Smagorinsky[7], WALE[8], WALE-similarity[9], SVV[10]. Filters: Vasilyev[11,12], discrete Gaussian[13], Modal Vandermonde[14].

E. Computing Architecture and Scalability

The Hi-FiLES code has been designed to work on multi-CPU as well as multi-CPU-GPU platforms. The Flux Reconstruction method in its current form with explicit time-stepping has a great potential for parallelization. Since the solution points are not explicitly shared between elements, most of the computations are element-local enabling an efficient use of shared memory on GPUs. Also, several computations are independent for each solution point and the highly parallelizable nature of GPUs becomes very useful. A detailed description of the paralleization of the FR method, along with scalability and performance analysis has been performed in[1].

F. Shock capturing and Stabilization Models

Currently, we have adapted Persson and Peraire's method[15] for shock detection and capturing. The method works well for inviscid flow cases and compressible flows upto a Mach number of 2 have been tried and tested. However the method requires fine-tuning of parameters for each problem and we are currently working on a new method which is more robust. Persson and Peraire have used this shock capturing tool as a stabilization method as well in their turbulence calculations and we plan to test this and present results for inviscid and viscous cases in the final draft. Here we show a few inviscid results for the case of M = 1.6 where we illustrate the ability to detect shocks and add dissipation in a local manner in the form of artificial viscosity in order to capture the shock in a fine manner and avoid the loss of accuracy away from the shock.

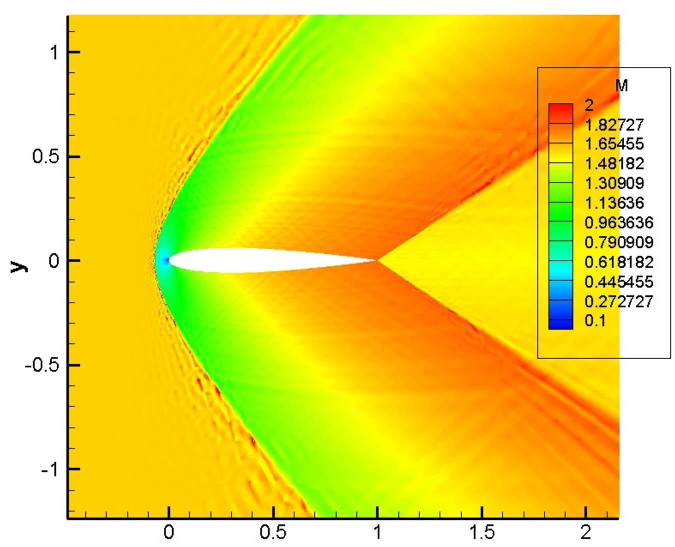

Figure 1: Mach contours for inviscid flow over Naca0012 at M = 1.6 and AoA = 0°

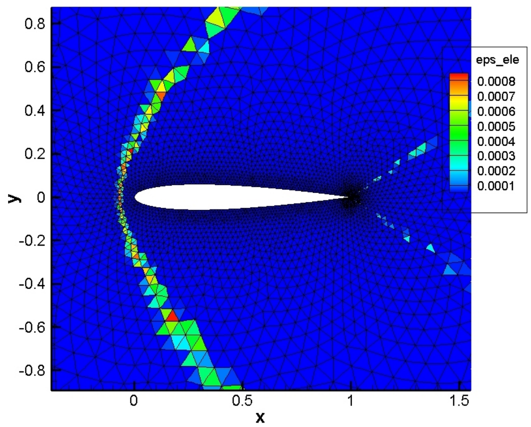

Figure 2: Element-wise AV co-efficients (case 1)

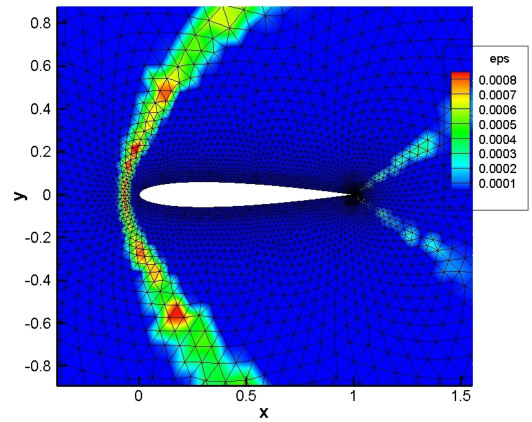

Figure 3: AV co-efficients with continuity enforcement

IV. Verification

This section describes the check of spatial and temporal order of accuracy using the Method of Manufactured Solutions in 2D and 3D for viscous and inviscid flows, characterization of stable time-step limits, assessment of computational cost per degree of freedom for a given error tolerance, and measurement of weak and strong scalability in GPUs and CPUs.

A. Method of Manufactured Solutions

c, κ	Grid	L_2 err.	L_{2s} err.	$O(L_2)$	$O(L_{2s})$
c_{dg}, κ_{dg}	$N = 24$	8.53e-04	1.43e-01		
	$N = 32$	3.60e-04	7.95e-02	2.98	2.00
	$N = 48$	1.01e-04	3.30e-02	3.16	2.18
	$N = 64$	3.98e-05	1.72e-02	3.27	2.30
c_+, κ_+	$N = 24$	5.65e-03	7.23e-01		
	$N = 32$	2.34e-03	4.12e-01	3.07	1.99
	$N = 48$	6.41e-04	1.79e-01	3.19	2.09
	$N = 64$	2.48e-04	9.61e-02	3.30	2.21

Figure 4: Accuracy of ESFR schemes for flow generated by a time-dependent source term on triangular grids, for the case of $p = 2$. The inviscid and viscous numerical fluxes were computed using a Rusanov flux with $\lambda = 1$ and a LDG flux with $\tau = 0.1$ and $\beta = \pm 0.5n$.

c, κ	Grid	L_2 err.	L_{2s} err.	$O(L_2)$	$O(L_{2s})$
c_{dg}, κ_{dg}	$N = 24$	1.27e-05	4.49e-03		
	$N = 32$	4.02e-06	1.86e-03	3.99	3.06
	$N = 48$	7.99e-07	5.35e-04	3.97	3.06
	$N = 64$	2.54e-07	2.26e-04	3.96	2.99
c_+, κ_+	$N = 24$	9.48e-05	1.71e-02		
	$N = 32$	2.86e-05	6.87e-03	4.17	3.16
	$N = 48$	5.27e-06	1.91e-03	4.17	3.15
	$N = 64$	1.58e-06	7.73e-04	4.18	3.15

Figure 5: Accuracy of ESFR schemes for flow generated by a time-dependent source term on triangular grids, for the case of $p = 3$. The inviscid and viscous numerical fluxes were computed using a Rusanov flux with $\lambda = 1$ and a LDG flux with $\tau = 0.1$ and $\beta = \pm 0.5n$.

	$p = 2$	$p = 3$
c_{dg}, κ_{dg}	2.67e-03	1.70e-03
c_+, κ_+	4.39e-03	2.35e-03

Figure 6: Explicit time-step limits (Δt_{max}) of ESFR schemes for flow generated by a time-dependent source term on the triangular grid with $\tilde{N} = 48$, for the cases of $p = 2 and 3$. The inviscid and viscous numerical fluxes were computed using a Rusanov flux with $\lambda = 1$ and a LDG flux with $\tau = 0.1$ and $\beta = \pm 0.5n$.

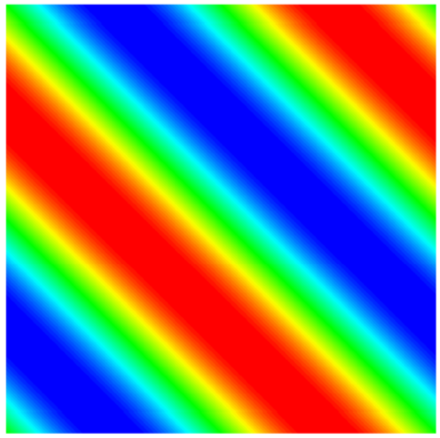

Figure 7: Contours of energy obtained using the ESFR scheme with $c = c_+$ and $\kappa = \kappa_+$ on the triangular grid with $\tilde{N} = 32$ for the case of $p = 3$. The inviscid and viscous numerical fluxes were computed using a Rusanov flux with $\lambda = 1$ and a LDG flux with $\tau = 0.1$ and $\beta = \pm 0.5n$.

c, κ	Grid	L_2 err.	L_{2s} err.	$O(L_2)$	$O(L_{2s})$
c_{dg}, κ_{dg}	$N = 24$	2.81e-03	4.98e-01		
	$N = 32$	1.20e-03	2.78e-01	2.95	2.03
	$N = 48$	3.58e-04	1.20e-01	2.99	2.07
	$N = 64$	1.48e-04	6.54e-02	3.07	2.11
c_+, κ_+	$N = 24$	1.05e-01	1.06e+01		
	$N = 32$	4.85e-02	6.45e+00	2.68	1.72
	$N = 48$	1.53e-02	3.02e+00	2.85	1.87
	$N = 64$	6.40e-03	1.69e+00	3.03	2.02

Figure 8: Accuracy of ESFR schemes for flow generated by a time-dependent source term on tetrahedral grids, for the case of $p = 2$. The inviscid and viscous numerical fluxes were computed using a Rusanov flux with $\lambda = 1$ and a LDG flux with $\tau = 0.1$ and $\beta = \pm 0.5n$.

c, κ	Grid	L_2 err.	L_{2s} err.	$O(L_2)$	$O(L_{2s})$
c_{dg}, κ_{dg}	$N = 24$	8.78e-05	2.24e-02		
	$N = 32$	2.70e-05	9.11e-03	4.11	3.13
	$N = 48$	5.17e-06	2.57e-03	4.07	3.12
	$N = 64$	1.62e-06	1.06e-03	4.04	3.10
c_+, κ_+	$N = 24$	3.86e-03	4.90e-01		
	$N = 32$	1.29e-03	2.17e-01	3.80	2.84
	$N = 48$	2.62e-04	6.51e-02	3.94	2.96
	$N = 64$	8.14e-05	2.69e-02	4.06	3.08

Figure 9: Accuracy of ESFR schemes for flow generated by a time-dependent source term on tetrahedral grids, for the case of $p = 3$. The inviscid and viscous numerical fluxes were computed using a Rusanov flux with $\lambda = 1$ and a LDG flux with $\tau = 0.1$ and $\beta = \pm 0.5n$.

	$p = 2$	$p = 3$
c_{dg}, κ_{dg}	1.07e-03	7.35e-04
c_+, κ_+	1.81e-03	1.03e-03

Figure 10: Explicit time-step limits (Δt_{max}) of ESFR schemes for flow generated by a time-dependent source term on the triangular grid with $\tilde{N} = 48$, for the cases of $p = 2 and 3$. The inviscid and viscous numerical fluxes were computed using a Rusanov flux with $\lambda = 1$ and a LDG flux with $\tau = 0.1$ and $\beta = \pm 0.5n$.

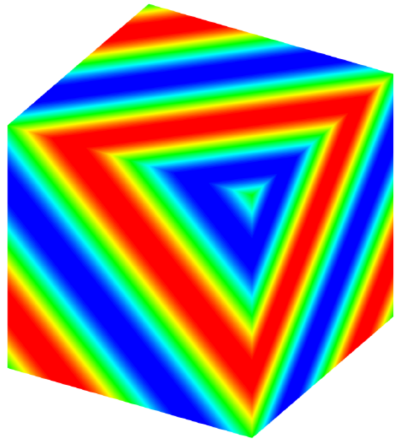

Figure 11: Contours of energy obtained using the ESFR scheme with $c = c_+$ and $\kappa = \kappa_+$ on the tetrahedral grid with $\tilde{N} = 32$ for the case of $p = 3$. The inviscid and viscous numerical fluxes were computed using a Rusanov flux with $\lambda = 1$ and a LDG flux with $\tau = 0.1$ and $\beta = \pm 0.5n$.

V. Validation

A. Flat Plate

Computations of the flow over a flat plate have been performed and validated against the results from the high-order workshop. We obtained a C_d value of 1.3112e-3 matching with results from the workshop. A detailed description of convergence and error vs. work-units will be presented in the final draft.

B. Circular Cylinder

c, κ	$M = 0.3$ $\overline{C_D}$	St	$M = 0.5$ $\overline{C_D}$	St
c_{dg}, κ_{dg}	1.3928	0.190	1.5669	0.190
c_+, κ_+	1.3923	0.190	1.5666	0.190

Figure 12: Values of the time-averaged drag coefficient and Strouhal number for the circular cylinder in flows with $M = 0.3$ and $M = 0.5$. The flows were simulated using the VCJH schemes with $p = 2, c = c_{dg}, \kappa = \kappa_{dg} and c = c_+, \kappa = \kappa_+$ in conjunction with the Rusanov flux with $\lambda = 1$ and the LDG flux with $\beta = 0.5n$ and $\tau = 0.1$ on the unstructured triangular grid with $N = 63472$ elements.

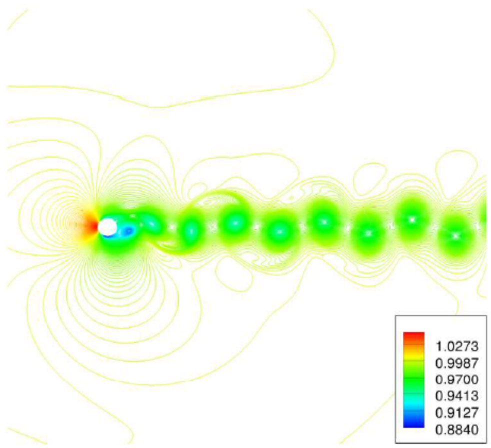

Figure 13: Density contour for the flow with $M = 0.3$ around the circular cylinder.

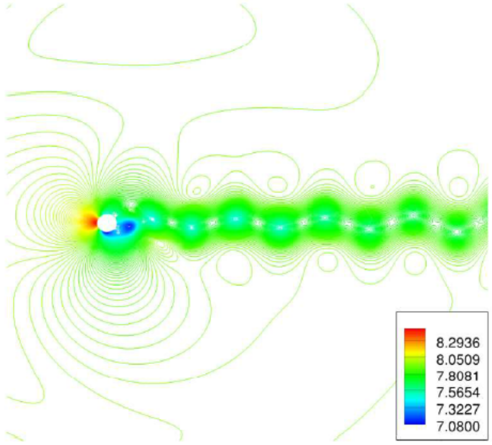

Figure 14: Pressure contour for the flow with $M = 0.3$ around the circular cylinder.

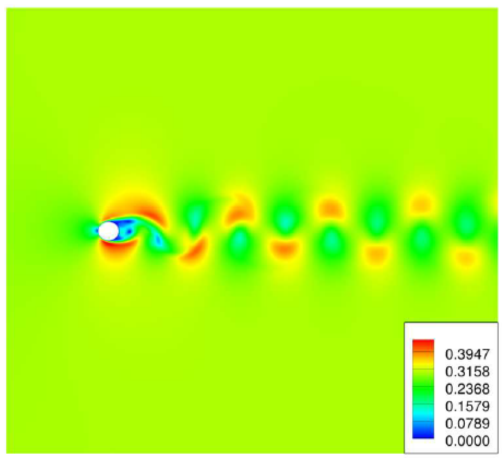

Figure 15: Mach contour for the flow with $M = 0.3$ around the circular cylinder.

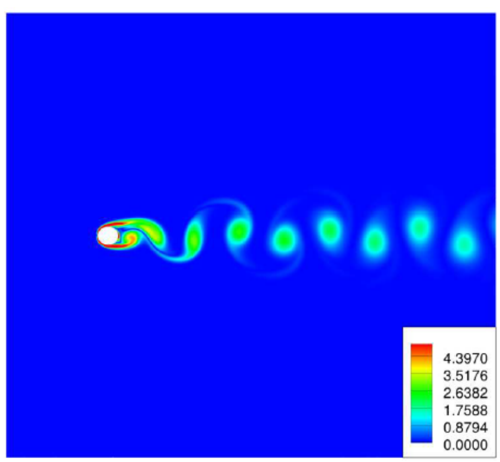

Figure 16: Vorticity contour for the flow with $M = 0.3$ around the circular cylinder.

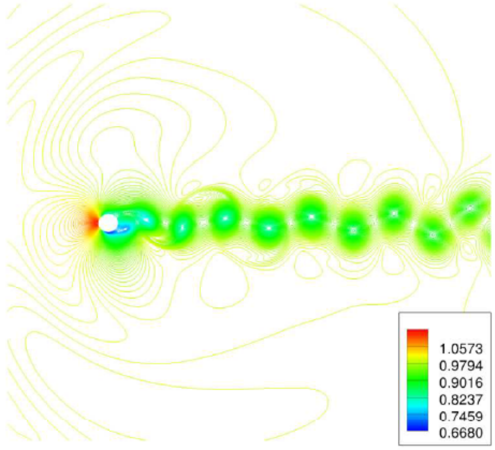

Figure 17: Density contour for the flow with $M = 0.5$ around the circular cylinder.

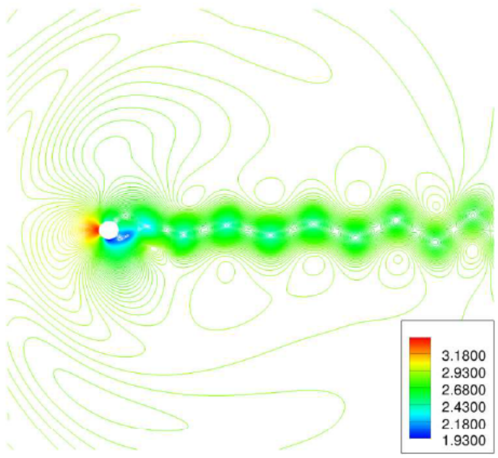

Figure 18: Pressure contour for the flow with $M = 0.5$ around the circular cylinder.

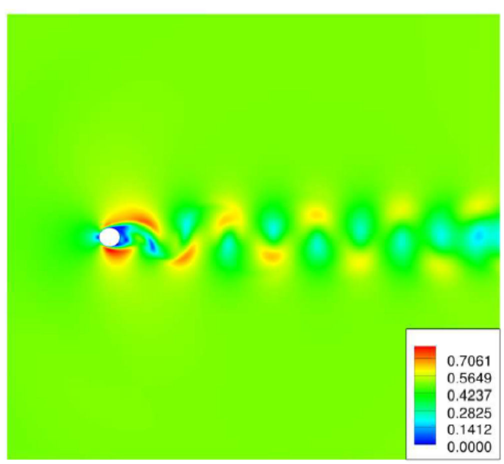

Figure 19: Mach contour for the flow with $M = 0.5$ around the circular cylinder.

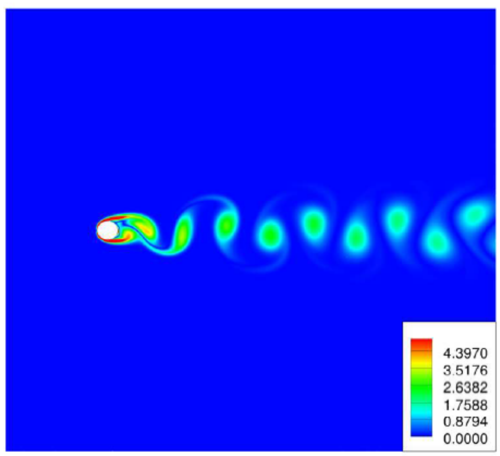

Figure 20: Vorticity contour for the flow with $M = 0.5$ around the circular cylinder.

C. SD7003 airfoil at 4° angle of attack

From Williams's thesis [16]

Source	$Re = 10\text{K}$ $\overline{C_L}$	$\overline{C_D}$	$Re = 22\text{K}$ $\overline{C_L}$	$\overline{C_D}$	$Re = 60\text{K}$ $\overline{C_L}$	$\overline{C_D}$
Uranga et al. [115]	0.3755	0.04978	0.6707	0.04510	0.5730	0.02097
c_{dg}, κ_{dg}	0.3719	0.04940	0.6722	0.04295	0.5831	0.01975
c_+, κ_+	0.3713	0.04935	0.6655	0.04275	0.5774	0.02005

Figure 21: Time-averaged values of the lift and drag coefficients for the SD7003 airfoil flows with $Re = 10000, 22000, 60000$

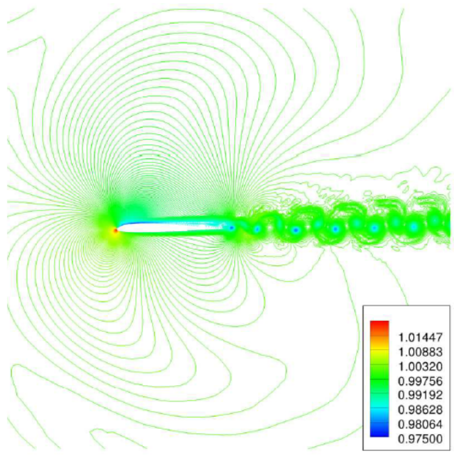

Figure 22: Density contour for the flow with $Re = 10000$ around the SD7003 airfoil.

D. SD7003 wing section at 4° angle of attack

From David's thesis.

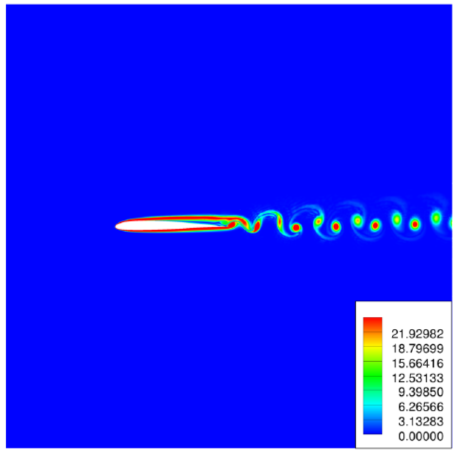

Figure 23: Vorticity contour for the flow with $Re = 10000$ around the SD7003 airfoil.

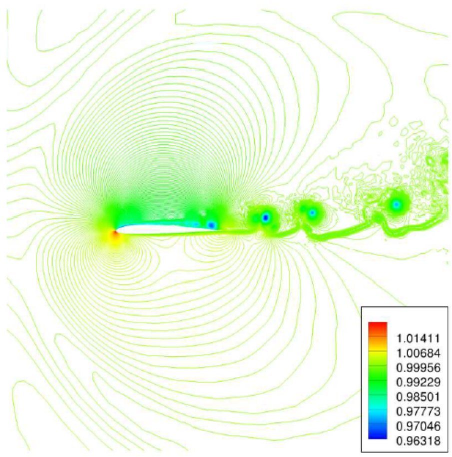

Figure 24: Density contour for the flow with $Re = 22000$ around the SD7003 airfoil.

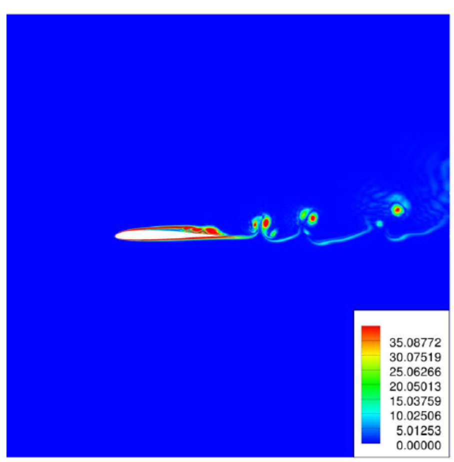

Figure 25: Vorticity contour for the flow with $Re = 22000$ around the SD7003 airfoil.

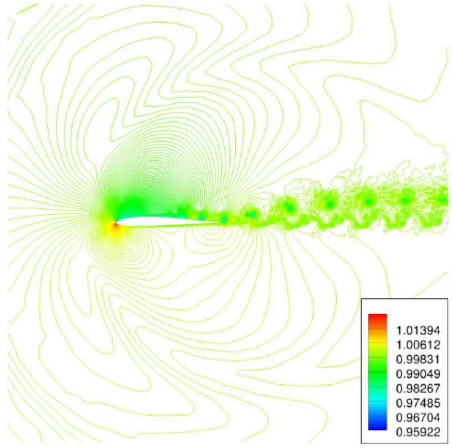

Figure 26: Density contour for the flow with $Re = 60000$ around the SD7003 airfoil.

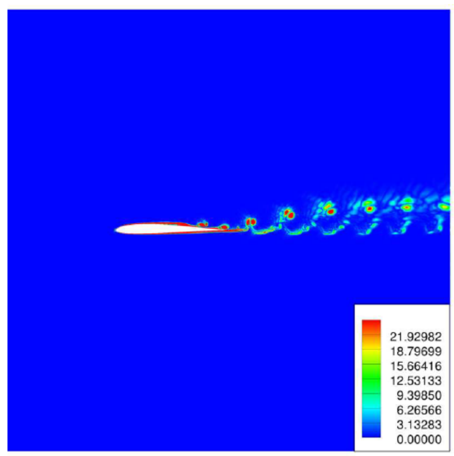

Figure 27: Vorticity contour for the flow with $Re = 60000$ around the SD7003 airfoil.

Source	$Re = 10\text{K}$ $\overline{C_L}$	$\overline{C_D}$
Uranga et al. [115]	0.3743	0.04967
c_{dg}, κ_{dg}	0.3466	0.04908
c_+, κ_+	0.3454	0.04903

Figure 28: Time-averaged values of the lift and drag coefficients for the SD7003 wing-section in a flow with $Re = 10000$

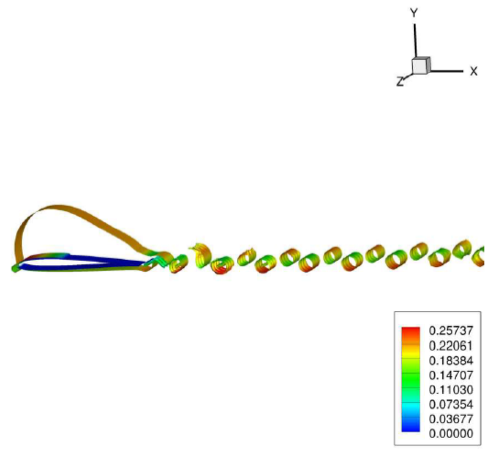

Figure 29: Density isosurfaces colored by Mach number for the flow with $Re = 10000$ around the SD7003 wing-section.

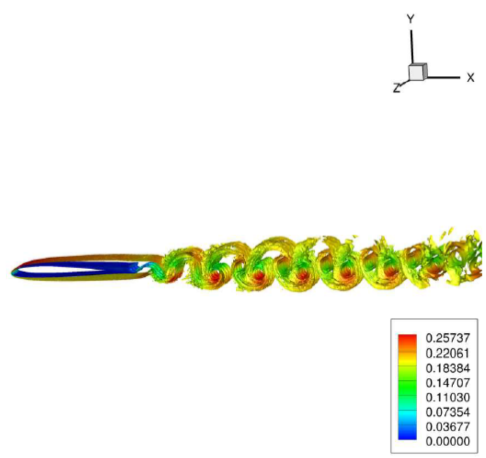

Figure 30: Vorticity isosurfaces colored by Mach number for the flow with $Re = 10000$ around the SD7003 wing-section.

E. Taylor-Green Vortex at Re = 1,600

The Taylor-Green Vortex (TGV) is a simple test of the ability of a numerical method to resolve the important dynamics of a turbulent flow. The compressible TGV at $Re = 1600$ was one of the benchmark problems in the 1st and 2nd International Workshops on High-Order CFD Methods[17,18], from which reference solutions are available, namely, fourth-order DG computations on a mesh of 64^3 elements[19] and DNS using a high-order compact difference scheme on a mesh of 512^3 elements[20]. The results presented here were obtained by Bull and Jameson using FR to recover the fourth-order-accurate SD scheme in HiFiLES[21,22]. From a simple initial condition in a triply-periodic box of dimensions $[-\pi : pi]^3$, interactions between vortices cause the flow to develop in a prescribed manner into a mass of elongated vortices across a range of scales. The initial condition is specified as

$$u(t_0) = u_0 \sin(x/L)\cos(y/L)\cos(z/L), \tag{7}$$

$$v(t_0) = -u_0 \cos(x/L)\sin(y/L)\cos(z/L), \tag{8}$$

$$w(t_0) = 0, \tag{9}$$

$$p(t_0) = p_0 + \frac{\rho_0 V_0^2}{16}\left[\cos\left(\frac{2x}{L}\right) + \cos\left(\frac{2y}{L}\right)\right]\left[\cos\left(\frac{2z}{L}\right) + 2\right], \tag{10}$$

where $L = 1$, $u_0 = 1$, $\rho_0 = 1$ and $p_0 = 100$. The Mach number is set to 0.08 (consistent with the initial pressure p_0) and the initial temperature is 300K.

Figs. 31 (a) and (b) show the volume-averaged kinetic energy $\langle k \rangle$ on (a) hexahedral meshes of 16^3, 32^3 and 64^3 elements and (b) tetrahedral meshes (formed by splitting the hexahedral meshes). Figs. 31 (c) and (d) show the kinetic energy dissipation rate, given by $\epsilon = -d\langle k \rangle/dt$. On the finest mesh the kinetic energy and dissipation rate predictions match the DNS data[20] and the high-order DG results at equal resolution[19]. These results show that the high-order numerical scheme is able to resolve the important flow dynamics on a relatively coarse mesh. As a qualitative measure of the resolution of the turbulent flow structures, Figure 32 shows isosurfaces of the q criterion at four times during the simulation. The evolution of complex small scale structures is evident.

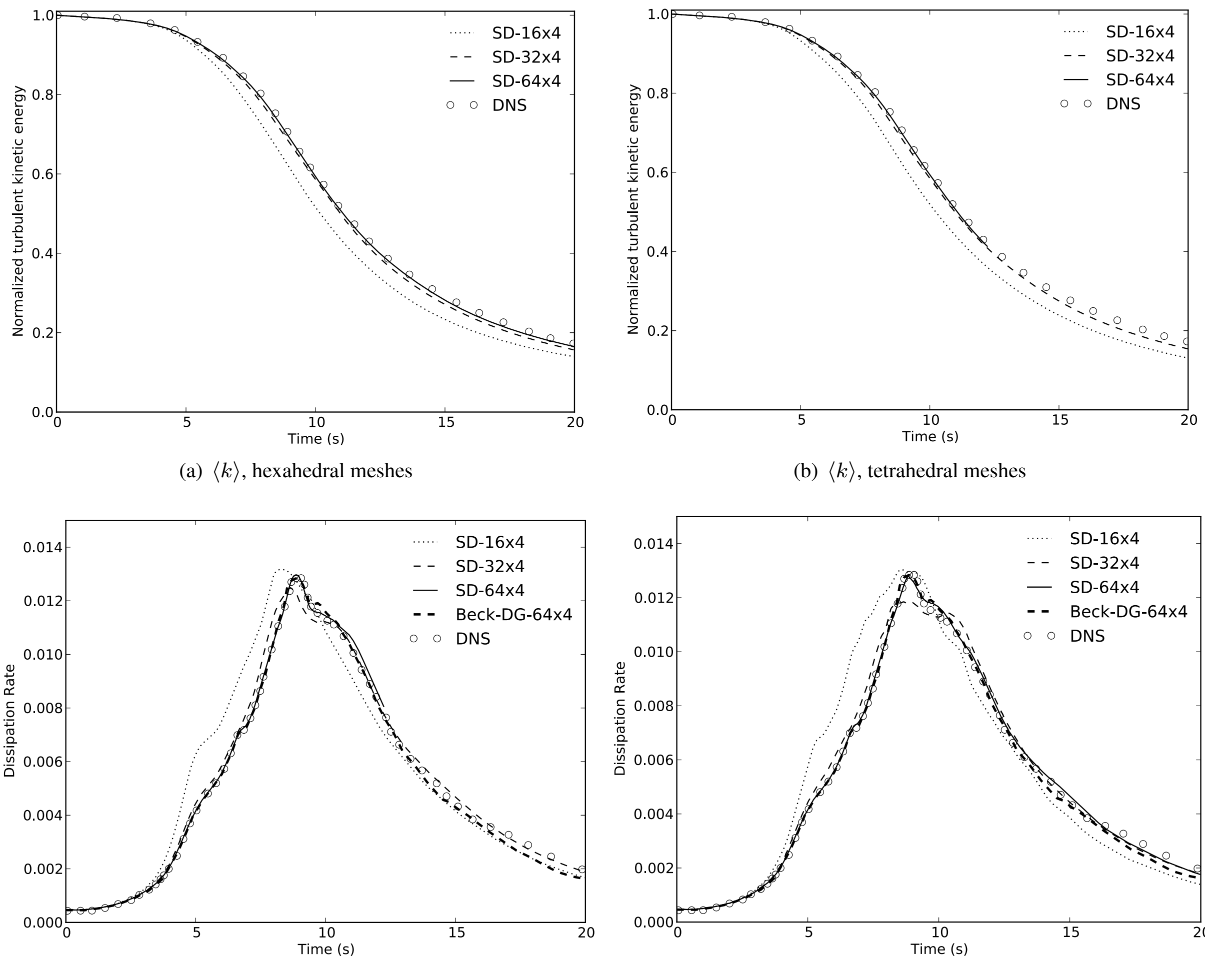

(a) $\langle k \rangle$, hexahedral meshes

(b) $\langle k \rangle$, tetrahedral meshes

(c) $-d\langle k \rangle/dt$, hexahedral meshes

(d) $-d\langle k \rangle/dt$, tetrahedral meshes

Figure 31: Taylor-Green vortex results on tetrahedral meshes. (a) Evolution of average kinetic energy $\langle k \rangle$. Dissipation rate $-d\langle k \rangle/dt$ with different (b) meshes and (c) orders. (d) Isosurface of Q-criterion at 10.75 seconds on 64^3 mesh at 4th order, showing vortex filaments. 'SD-$M \times N$' refers to M^3 mesh, Nth-order accurate SD scheme. (**- - -**) 4th-order DG on 64^3 mesh[19]; (○) DNS[20].

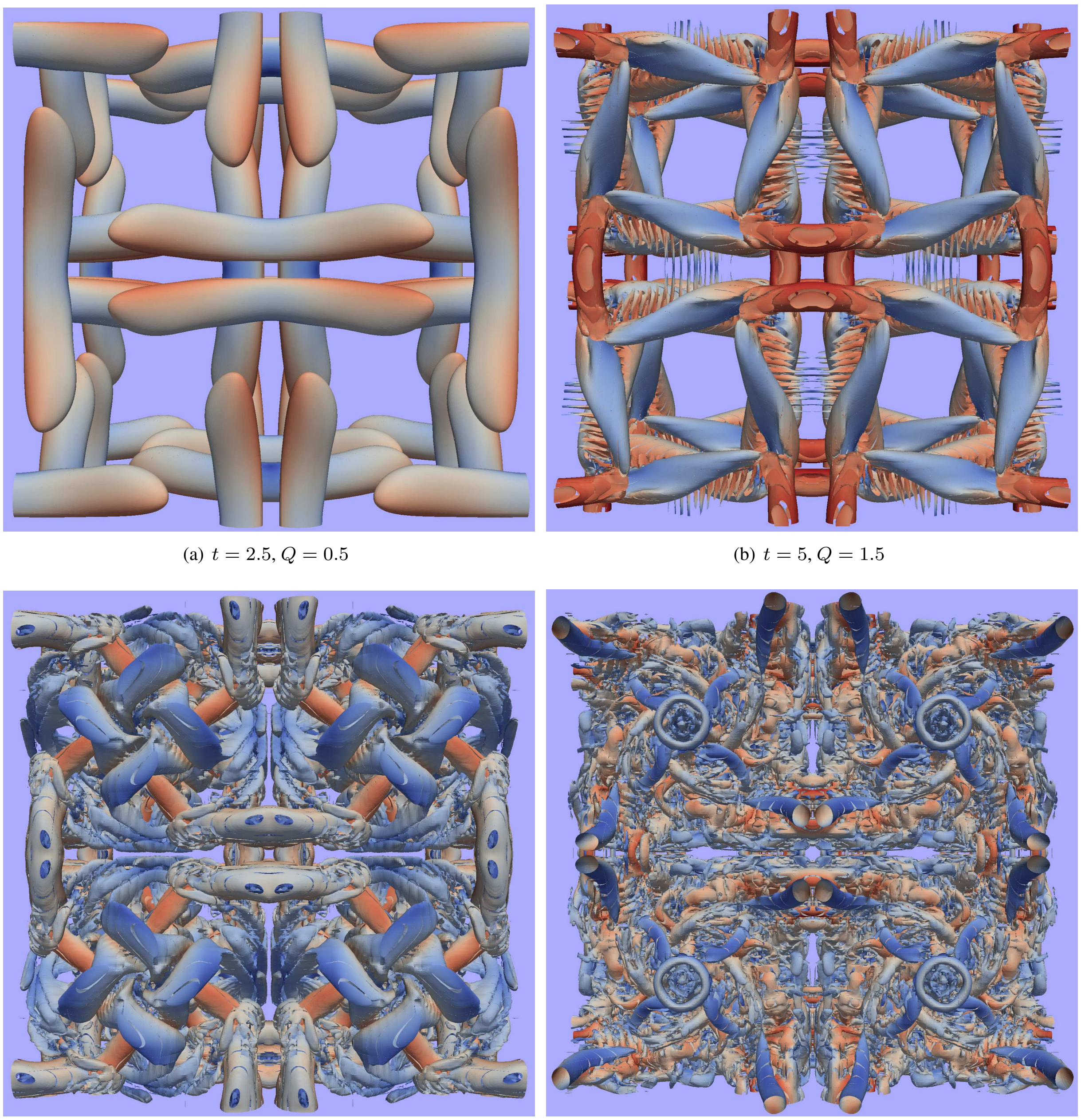

(a) $t = 2.5, Q = 0.5$

(b) $t = 5, Q = 1.5$

(c) $t = 7.5, Q = 1.5$

(d) $t = 10.75, Q = 1.5$

Figure 32: TGV solution on the fine mesh using fourth order accurate DG method, showing isosurfaces of q criterion colored by velocity magnitude at time t = 2.5 to 10.75 seconds.

VI. Conclusion

Conclusions here...

Acknowledgements

The authors would like to acknowledge the support for this work provided by the Stanford Graduate Fellowships, National Science Foundation Graduate Fellowships, and the Air Force Office of Scientific Research.

References

[1]Castonguay, P., Williams, D., Vincent, P., López-Morales, M. R., and Jameson, A., "On the Development of a High-Order, Multi-GPU Enabled, Compressible Viscous Flow Solver for Mixed Unstructured Grids," *AIAA Computational Fluid Dynamics Conference, AIAA-2011-3229*, 2011.

[2]Castonguay, P., Vincent, P. E., and Jameson, A., "A new class of high-order energy stable flux reconstruction schemes for triangular elements," *Journal of Scientific Computing*, Vol. 51, No. 1, 2012, pp. 224–256.

[3]Williams, D., Castonguay, P., Vincent, P., and Jameson, A., "Energy Stable Flux Reconstruction Schemes for Advection-Diffusion Problems on Triangles," *Journal of Computational Physics*, 2013.

[4]Williams, D. and Jameson, A., "Energy Stable Flux Reconstruction Schemes for Advection–Diffusion Problems on Tetrahedra," *Journal of Scientific Computing*, 2013, pp. 1–39.

[5]Fidkowski, K. J., Oliver, T. A., Lu, J., and Darmofal, D. L., "p-Multigrid solution of high-order discontinuous Galerkin discretizations of the compressible Navier–Stokes equations," *Journal of Computational Physics*, Vol. 207, No. 1, 2005, pp. 92–113.

[6]Jameson, A., "Time Dependent Calculations Using Multigrid, with Applications to Unsteady Flows Past Airfoils and Wings," *Proc. 10th Comp. Fluid Dyn. Conf., Honolulu, HI, USA, June 24-26, 1991, AIAA-Paper 91-1596*, 1991.

[7]Smagorinsky, J., "General circulation experiments with the primitive equations," *Monthly Weather Review*, Vol. 91, No. 3, 1963, pp. 99–164.

[8]Nicoud, F. and Ducros, F., "Subgrid-Scale Stress Modelling Based on the Square of the Velocity Gradient Tensor," Vol. 62, No. 3, Sept. 1999, pp. 183–200.

[9]Lodato, G., Vervisch, L., and Domingo, P., "A Compressible Wall-Adapting Similarity Mixed Model for Large-Eddy Simulation of the Impinging Round Jet," Vol. 21, No. 3, 2009.

[10]Karamanos, G. and Karniadakis, G., "A spectral vanishing viscosity method for large-eddy simulations," *J. Comput. Phys.*, Vol. 163, No. 1, 2000, pp. 22–50.

[11]Vasilyev, O. V., Lund, T. S., and Moin, P., "A General Class of Commutative Filters for LES in Complex Geometries," *Journal of Computational Physics*, Vol. 146, 1998, pp. 82–104.

[12]Vasilyev, O. V., Marsden, A. L., and Moin, P., "Construction of Commutative Filters for LES on Unstructured Meshes," *Journal of Computational Physics*, Vol. 175, 2002, pp. 584–603.

[13]Lodato, G., Castonguay, P., and Jameson, A., "Discrete filter operators for large-eddy simulation using high-order spectral difference methods," *Int. J. Numer. Meth. Fl.*, Vol. in press, 2012.

[14]Blackburn, H. and Schmidt, S., "Spectral element filtering techniques for large eddy simulation with dynamic estimation," *Journal of Computational Physics*, Vol. 186, 2003, pp. 610–629.

[15]Persson, P. and Peraire, J., "Sub-Cell Shock Capturing for Discontinuous Galerkin Methods," Tech. rep., 2006.

[16]Williams, D. M., *Energy Stable High-Order Methods for Simulating Unsteady, Viscous, Compressible Flows on Unstructured Grids*, Ph.D. thesis, Stanford University, 2013.

[17]"1st International Workshop on High-order CFD methods," At the 50th AIAA Aerospace Sciences Meeting, January 7-8 2012, Nashville, Tennessee, January 2012.

[18]"2nd International Workshop on High-order CFD methods," At DLR, May 27-28, Cologne, Germany, May 2013.

[19]Beck, A. and Gassner, G., "On the accuracy of high-order discretizations for underresolved turbulence simulations," *Theoretical and Computational Fluid Dynamics*, Vol. 27, No. 3-4, 2012, pp. 221–237.

[20]Debonis, J., "Solutions of the Taylor-Green Vortex Problem Using High-Resolution Explicit Finite Difference Methods," *AIAA Paper 2013-0382*, 2013.

[21]Bull, J. and Jameson, A., "On the use of high-order Flux Reconstruction schemes for implicit large eddy simulation of turbulent flows," unpublished.

[22]Bull, J. and Jameson, A., "On the use of high-order Flux Reconstruction schemes for implicit large eddy simulation of turbulent flows," *Notes on Numerical Fluid Mechanics and Multidisciplinary Design, Vol.*, edited by W. Haasse, Springer, May 2014, unpublished.